Unveiling the electrochemical mechanisms of the Li 2 Fe(SO 4) 2 polymorphs by neutron diffraction and density functional theory calculations

Laura Lander, Marine Reynaud, Javier Carrasco, Nebil A. Katcho, Christophe Bellin, Alain Polian, Benoît Baptiste, Gwenaëlle Rousse, Jean-marie Tarascon

Unveiling the electrochemical mechanisms of the $Li_2Fe(SO_4)_2$ polymorphs by neutron diffraction and density functional theory calculations

Laura Lander[a,b,c], Marine Reynaud[d], Javier Carrasco[d], Nebil A. Katcho[d], Christophe Bellin[c,e], Alain Polian[c,e], Benoît Baptiste[c,e], Gwenaëlle Rousse[a,b,c], Jean-Marie Tarascon*[a,b,c]

[a] FRE 3677 "Chimie du Solide et Energie", Collège de France, 11 Place Marcelin Berthelot, 75231 Paris Cedex 05, France

[b] Réseau sur le Stockage Electrochimique de l'Energie (RS2E), FR CNRS 3459, France

[c] Sorbonne Universités - UPMC Univ Paris 06, 4 Place Jussieu, 75005 Paris, France

[d] CIC Energigune, Parque Tecnológico de Álava, C/ Albert Einstein 48, 01510 Miñano (Vitoria, Álava), Spain

[e] IMPMC, CNRS, UMR 7590, 4 Place Jussieu, 75005 Paris, France

* Corresponding author: jean-marie.tarascon@college-de-france.fr

Manuscript

Abstract

The quest for new sustainable iron-based positive electrode materials for lithium-ion batteries recently led to the discovery of a new family of compounds with the general formula $Li_2M(SO_4)_2$, which presents monoclinic and orthorhombic polymorphs. In terms of electrochemical performances, although both $Li_2Fe(SO_4)_2$ polymorphs present a similar potential of ~3.8 V vs Li^+/Li^0, the associated electrochemical processes drastically differ in terms of polarization and reaction redox mechanisms. We herein provide an explanation to account for such a behavior. While monoclinic $Li_2Fe(SO_4)_2$ directly transforms into $Li_{1.0}Fe(SO_4)_2$ upon oxidation, the orthorhombic counterpart forms a distinct intermediate $Li_{1.5}Fe(SO_4)_2$ phase leading to a two-step delithiation process involving an unequal depopulation of the two Li sites pertaining to the structure as deduced by neutron powder diffraction experiments and confirmed by both density functional theory and Bond Valence Energy Landscape calculations. Moreover, to access band gap information, both polymorphs are studied by UV/Vis spectroscopy. Lastly, the possibility to transform the monoclinic phase to the orthorhombic phase via pressure is explored.

Keywords

Introduction

Over the last few decades, lithium-ion batteries have conquered the portable electronics market and are amongst the best contenders for electric vehicles and grid storage technologies due to their attractive energy densities and cycling properties. However, these latter applications call for cathode materials improvements in terms of sustainability, cost and safety performances.[1] This demand has led to the development of the polyanionic iron-based $LiFePO_4$ phase, which shows a potential of 3.45 V vs Li^+/Li^0 together with positive safety and cost attributes.[2] Such a finding triggered a growing interest for polyanionic materials, owing to the ability to tune their redox potential by changing the nature of the polyanionic group and hence the iono-covalency of the metal-anion group.[3] Implementing this inductive effect described by Goodenough *et al.*[3] led to the discovery of a variety of new iron-based polyanionic compounds, such as $LiFeBO_3$,[4–6] Li_2FeSiO_4[7–10] as well as the fluorosulfate family $AMSO_4F$ (with A=Li, Na and M= Mn, Fe) explored by our group with the most prominent members being *tavorite* and *triplite* $LiFeSO_4F$, which show a working potential of 3.6 V and 3.9 V vs Li^+/Li^0, respectively.[11–15]

Searching for further high potential materials that circumvent the use of toxic fluorine, our group successfully synthesized the family of bimetallic sulfates $A_2M(SO_4)_2$ (with A= Li, Na and M= Mn, Fe, Co, Ni, Zn), where especially the monoclinic *marinite* $Li_2Fe(SO_4)_2$ phase has generated great interest due to its elevated Fe^{3+}/Fe^{2+} redox potential (~ 3.83 V vs Li^+/Li^0).[16–20] Our group has further shown the existence of a polymorphism within these $Li_2M(SO_4)_2$ phases, with the $Li_2M(SO_4)_2$ (M = Fe, Co, Ni, Zn) compounds being able to crystallize in an orthorhombic structure by changing the synthesis conditions, namely the use of a ball-milling route as opposed to the ceramic route for the monoclinic polymorphs.[21] Herein, we are presenting a comparative study of the chemical, electrochemical and physical properties of the two $Li_2Fe(SO_4)_2$ polymorphs. The electrochemically-driven structural changes are investigated through a combination of experimental neutron powder diffraction and theoretical density functional theory (DFT) calculations, while the Bond Valence Energy Landscapes (BVEL) approach is used to explore the Li diffusion pathways for both $Li_2Fe(SO_4)_2$ polymorphs. Lastly, the optical properties namely the band gap of these materials are accessed via UV/Vis spectroscopy, and the effect of pressure on polymorphism is addressed.

Experimental

Syntheses

Orthorhombic phases: The synthesis of the orthorhombic compounds $Li_2Co(SO_4)_2$, $Li_2Zn(SO_4)_2$ and $Li_2Fe(SO_4)_2$ was performed by ball-milling stoichiometric amounts of anhydrous MSO_4 (M= Co, Zn, Fe) and Li_2SO_4 for several hours with a Retsch PM100 planetary mill. For $Li_2Co(SO_4)_2$ and $Li_2Zn(SO_4)_2$, the starting materials were ball-milled for 10 hours and 7 hours, respectively (divided into 30 min steps with 15 min pauses) under air atmosphere, whereas for $Li_2Fe(SO_4)_2$, the precursors were ball-milled for 5 hours under argon atmosphere in order to avoid the oxidation of Fe^{II+} to Fe^{III+}. Orthorhombic $Li_2Ni(SO_4)_2$ was obtained by a ceramic route, which includes ball-milling of stoichiometric ratios of Li_2SO_4 and $NiSO_4$ for 20 min using a Spex 8000 vibratory mill, pressing the resulting mixture into a pellet and heating at 500 °C for 24 hours.

The chemically oxidized phases $Li_{1.5}Fe(SO_4)_2$ and $Li_{1.0}Fe(SO_4)_2$ were obtained by stirring $Li_2Fe(SO_4)_2$ in acetonitrile with the respective molar amount of NO_2BF_4 as oxidizing agent at room temperature overnight. The reaction was conducted under inert atmosphere. The samples were then thoroughly washed with acetonitrile and dried under vacuum.

Monoclinic phases: Monoclinic $Li_2M(SO_4)_2$ (M = Mn, Fe and Co) phases were synthesized via a ceramic route, where first stoichiometric ratios of the sulfate precursors Li_2SO_4 and MSO_4 were ball-milled for 20 min using a Spex 8000M vibratory mill. The so-obtained mixtures were then pressed into pellets and annealed at different temperatures for different times, depending on the nature of the metal. Given the propensity of Fe^{II+} to oxidize, the second step was conducted in a silica tube sealed under vacuum at 320 °C for 72 hours. The monoclinic cobalt phase was obtained through heat treatment at 400 °C overnight and the manganese phase by heating for 4 days at 350 °C.

Characterizations

UV/Vis spectroscopy

UV/Vis spectroscopy was performed on the orthorhombic and monoclinic polymorphs of the $Li_2M^{II+}(SO_4)_2$ series with M^{II+}= Mn, Fe, Co, Ni, Zn with a Perkin Elmer Lambda 1050 spectrometer equipped with an integration sphere. The UV/Vis spectra were recorded between 180 and 2500 nm with a 1 nm step. The baseline was measured with a Spectralon reference.

4

X-ray and Neutron Powder Diffraction

The purity of the as-prepared samples was checked by laboratory powder X-Ray diffraction (XRD) using a Bruker D8 Advance diffractometer equipped with a copper source ($\lambda_{K\alpha1}$ = 1.54056 Å, $\lambda_{K\alpha2}$ = 1.54439 Å) and a LynxEye detector. High intensity neutron powder diffraction (NPD) was performed on the D20 diffractometer at the Institut Laue Langevin (ILL, Grenoble, France) in a high-resolution mode (Take-off angle of 90°) with a wavelength of λ = 1.544 Å.[22] NPD patterns were recorded at 100 K for the orthorhombic $Li_2Fe(SO_4)_2$ and at 30 K for its oxidized phases. Nuclear structures were refined using the Rietveld method as implemented in the FullProf program.[23–25] Fourier differential maps were generated using the GFourier program of the FullProf Suite.[25]

High-pressure experiments

Monoclinic $Li_2Co(SO_4)_2$ and $Li_2Mn(SO_4)_2$ were loaded in a membrane diamond anvil cell (DAC)[26] with a 400 μm culet diameter. We used a stainless steel gasket preindented to 45 μm, with a 200 μm hole and neon as a pressure transmitting medium.[27] Neon is the best suited pressure transmitting medium in our case since it ensures quasi hydrostatic conditions on the sample in the whole explored pressure range, it is chemically inert and has no Raman activity. The R1-line emission of a tiny ruby sphere was used as a pressure gauge.[28,29] The initial loading pressure accounts for 0.15 GPa and the pressure was gradually increased up to 5.65 GPa for $Li_2Co(SO_4)_2$ and 12.3 GPa for $Li_2Mn(SO_4)_2$.

The Raman experiments were carried out at 300 K in the back scattering configuration using a Jobin-Yvon HR-460 spectrometer equipped with a monochromator with 1,500 grooves/mm and an Andor CCD camera. Raman signal was excited using the 514.5 nm wavelength of an Ar laser, focused into a 2 μm spot by a long-working distance Mitutoyo x20 objective and collected in backscattering geometry. The power of the laser measured directly on the DAC was always kept below 2 mW in order to avoid any photo-induced transformation of the sample.[30,31]

Theoretical methods

Spin-polarized DFT calculations were performed using a supercell approach and the semi-local Perdew-Burke-Ernzerhof (PBE)[32] functional as implemented in the Vienna *ab initio* Simulation Package (VASP, version 5.3.3).[33,34] We replaced the inner electrons by PBE-based projector augmented wave potentials[35], whereas Li (2*s*), Fe (3*p*, 3*d*, 4*s*), S (3*s*, 3*p*) and O (2*s*, 2*p*) valence electrons were expanded in plane-waves with a cut-off energy of 700 eV. We employed the DFT+U scheme of Dudarev et al.[36], in which the

5

Hubbard U-like term (the difference between the Coulomb U and exchange J parameters, hereinafter referred to as simply U) was added to the exchange-correlation functional. This pragmatic approach is necessary to describe the localized Fe $3d$ states in $Li_xFe(SO_4)_2$ phases. Here, the chosen value of U is 4.0 eV, which is consistent with the value derived for a range of Fe-based cathode materials[37] and with the one used by Clark *et al*. to calculate open cell voltages for monoclinic *marinite* $Li_2Fe(SO_4)_2$.[38]

We used unit cells containing 8 formula units ($Li_xFe_8S_{16}O_{64}$). Equilibrium lattice parameters of bulk $Li_xFe(SO_4)_2$ were computed allowing the atomic positions, lattice constants and cell shape to relax with a residual force threshold of 0.02 eV/Å. We confirmed that the cut-off of 700 eV was sufficiently large to avoid the problems of Pulay stress and changes in basis set that accompany volume changes in plane wave calculations. We considered a 4×4×2 Monkhorst-Pack k-point mesh. These computational settings guarantee a tight convergence in total energies (better than 5 meV per formula unit) and equilibrium distances (better than 0.01 Å). We found that an antiferromagnetic ordering of the moments on all Fe atoms in $Li_2Fe(SO_4)_2$ is only 4 meV per formula unit lower in energy than a ferromagnetic ordering (high-spin states). We considered an antiferromagnetic structure similar to that proposed for orthorhombic $Li_2Ni(SO_4)_2$, where magnetic moments alternate orientations spin up and spin down along the *c*-axis, whereas the same spin orientation is maintained along *a*- and *b*-axis.[39] However, given the small energy difference between the two magnetic orderings, we restricted our calculations on all $Li_xFe(SO_4)_2$ phases to ferromagnetic ordering for the sake of simplicity.

We generated all the possible Li-vacancy arrangements within $Li_1Fe(SO_4)_2$ and $Li_{1.5}Fe(SO_4)_2$ cells using the cluster assisted statistical mechanics (CASM) code[40], which takes into account the symmetry of the lattice. We took the structure with the lowest energy as the ground-state structure. However, given the large number of possible Li-vacancy configurations, we applied a screening procedure by first computing the electrostatic energy using formal charges and the Ewald summation.[41] The 50 lowest electrostatic energy structures were then optimized using DFT. Similar two-step screening procedures have recently been applied to account, for example, for disordered Li sites in garnet electrolytes.[42,43]

Results/Discussion

Delithiation mechanisms of the $Li_2Fe(SO_4)_2$ polymorphs

In previous works, our group showed that the two $Li_2Fe(SO_4)_2$ polymorphs can reversibly release one Li from their structure and that this electrochemical activity occurs at high potentials of ~ 3.8 V vs. Li^+/Li^0.[16,21] However, although the structural frameworks of the two polymorphs show a similar local arrangement (both structures are based on a 3D network with isolated MO_6 octahedra connected to SO_4 tetrahedra via vertices, thus forming voids in which Li cations are located), their Li removal/insertion mechanisms present substantial differences (Figure 1). The monoclinic phase shows a much higher polarization than the orthorhombic one with in addition the presence of a single oxidation plateau between lithiated $Li_2Fe(SO_4)_2$ and delithiated $Li_{1.0}Fe(SO_4)_2$ (Figure 1a), as opposed to two successive plateaus for the orthorhombic polymorph. These two plateaus are associated with the existence of two different biphasic domains which share in common an intermediate phase of the well-defined composition $Li_{1.5}Fe(SO_4)_2$ (Figure 1b). The structural changes occurring between the lithiated and delithiated monoclinic phases were previously studied by neutron powder diffraction (NPD) and the determination of the structure of monoclinic $Li_{1.0}Fe(SO_4)_2$ revealed a reorganization of the Li atoms within the channels.[18] Here, we combine similarly experimental NPD measurements with theoretical DFT and BVEL calculations to study the Li-driven structural changes associated to the removal of Li from orthorhombic $Li_2Fe(SO_4)_2$.

a) Monoclinic Li₂Fe(SO₄)₂

b) Orthorhombic Li₂Fe(SO₄)₂
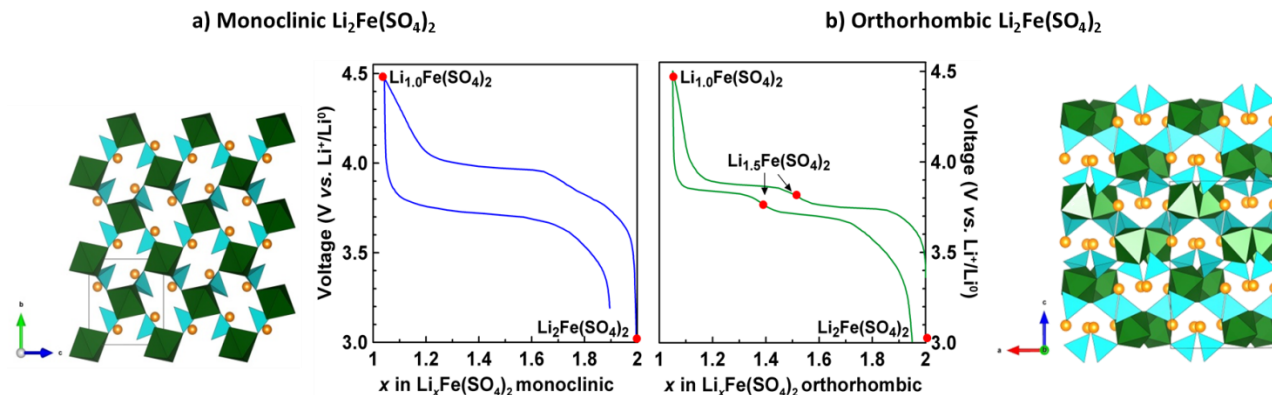
Figure 1: Structures and voltage-composition traces of a) monoclinic and b) orthorhombic $Li_2Fe(SO_4)_2$. The monoclinic curve displays one single plateau whereas the orthorhombic curve shows two successive biphasic processes with the formation of $Li_{1.5}Fe(SO_4)_2$ and $Li_{1.0}Fe(SO_4)_2$. MO_6 octahedra and SO_4 tetrahedra are displayed in green and blue, respectively. Lithium atoms are illustrated as orange balls.

The neutron powder diffraction patterns of the three orthorhombic phases $Li_2Fe(SO_4)_2$, $Li_{1.5}Fe(SO_4)_2$ and $Li_{1.0}Fe(SO_4)_2$ were recorded on the D20 diffractometer using a high-resolution configuration with a wavelength of 1.544 Å. $Li_2Fe(SO_4)_2$ can be refined with the structural model in the *Pbca* space group described in Ref. 21 (Figure 2a). In order to obtain a first hint for the lithium positions in the delithiated compounds, we created Fourier difference maps from the refinements of the NPD patterns of $Li_2Fe(SO_4)_2$, $Li_{1.5}Fe(SO_4)_2$ and $Li_{1.0}Fe(SO_4)_2$, where solely the $Fe(SO_4)_2$ framework was taken into account. A cross-section of these Fourier maps at z = 0.62 is shown in Figure 3. These maps are plotted so that the largest negative peaks are in blue, while intensities greater than zero are in yellow. The Fourier difference maps present negative domains that correspond to the coherent scattering length of Li (b_{Li}= –1.69 fm). For the pristine $Li_2Fe(SO_4)_2$ compound, the two crystallographically distinct Li1 and Li2 sites can be easily spotted, in agreement with the Rietveld refinement shown above. On delithiation, we notice that the Li1 site remains fully occupied, while the density of the Li2 atom gets weaker for the partially delithiated $Li_{1.5}Fe(SO_4)_2$ sample and finally vanishes for $Li_{1.0}Fe(SO_4)_2$. The impact of the lithium distribution in the framework was further evaluated by simulating neutron patterns with various occupation possibilities (occupied, half occupied, empty) for the Li1 and Li2 sites in $Li_{1.0}Fe(SO_4)_2$ (Figure 4). The biggest difference between the simulated patterns can be seen in the intensity of the first three peaks, where an empty Li1 site (orange pattern) leads to the highest intensity for the (102) peak (2θ = 16.3°) and the lowest intensity for the (112) and (200) peaks (2θ = 19.2°), while a delithiated Li2 site (green pattern) shows the reverse trend. The experimental $Li_{1.0}Fe(SO_4)_2$ pattern clearly looks similar to the latter. We therefore performed

the Rietveld refinements with a fully occupied Li1 site and a Li2 site that was fixed in the refinements to be either half occupied ($Li_{1.5}Fe(SO_4)_2$) or unoccupied ($Li_{1.0}Fe(SO_4)_2$). We used soft constraints for the S-O distances and angles, while the Li and Fe atomic positions were freely refined. Refining the occupancies of Li1 and Li2 did not change the outcome of the fit. The results of the Rietveld refinements are presented in Figure 2a-c and Table 1,Table 2 and Table 3.
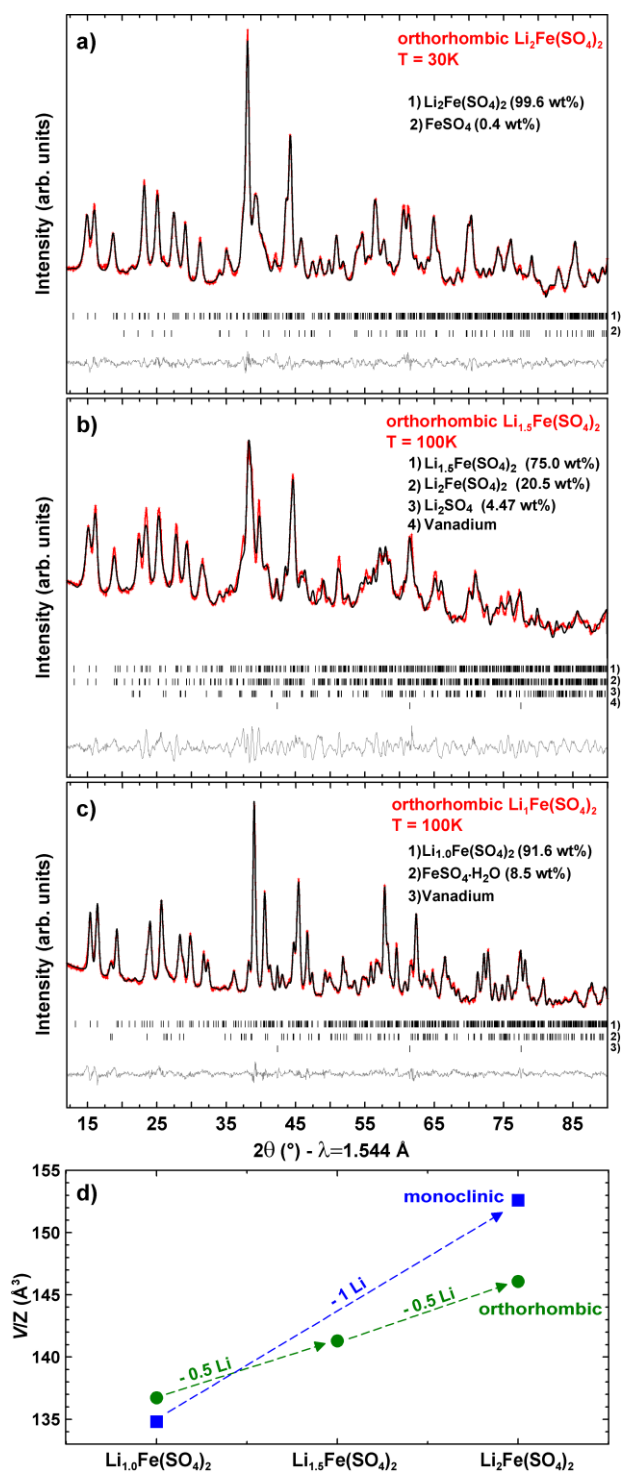
Figure 2: Rietveld refinements of neutron powder diffraction patterns of orthorhombic (a) $Li_2Fe(SO_4)_2$, (b) $Li_{1.5}Fe(SO_4)_2$ and (c) $Li_{1.0}Fe(SO_4)_2$ recorded on D20 at ILL using a wavelength of λ = 1.544 Å. The additional vanadium peaks stem from the sample container. (d) Evolution of the volume per formula unit for the orthorhombic (green) and monoclinic (blue) $Li_2Fe(SO_4)_2$, $Li_{1.5}Fe(SO_4)_2$ and $Li_{1.0}Fe(SO_4)_2$ phases.
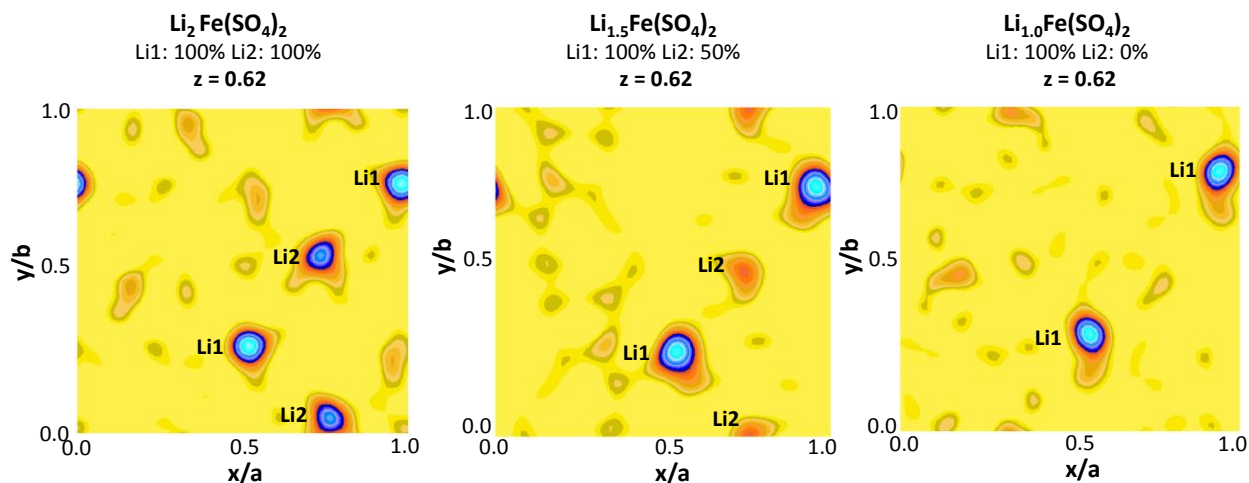
Figure 3: Difference Fourier maps plotted for z = 0.62, obtained from the refinement of the neutron powder diffraction patterns of the orthorhombic phases $Li_2Fe(SO_4)_2$, $Li_{1.5}Fe(SO_4)_2$ and $Li_{1.0}Fe(SO_4)_2$ by taking into account solely the $Fe(SO_4)_2$ framework. The light blue ellipsoids refer to a negative value and correspond to the positions of the missing lithium cations.
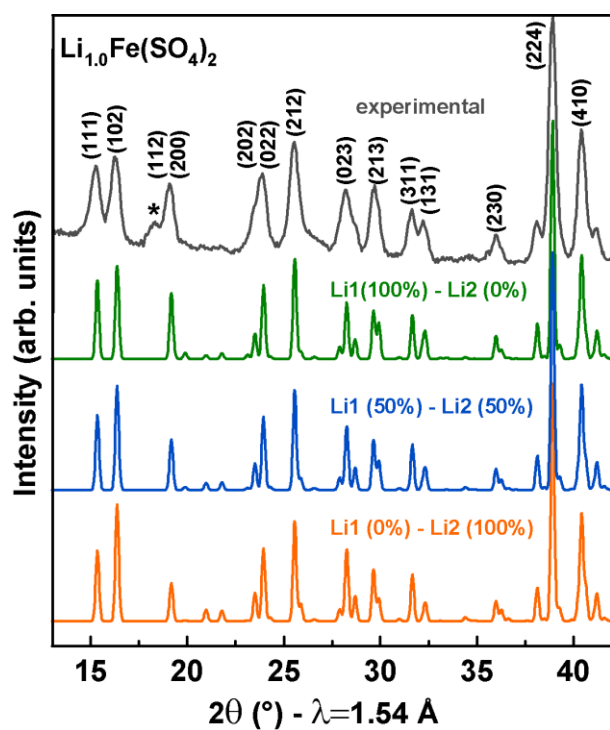
Figure 4: Simulation of patterns for $Li_{1.0}Fe(SO_4)_2$ with either an unoccupied Li1 site (orange pattern), an unoccupied Li2 site (green pattern) or equally occupied Li1/Li2 sites (blue pattern) and the experimental neutron powder diffraction pattern of $Li_{1.0}Fe(SO_4)_2$ (grey pattern). The star marks a peak attributed to an $FeSO_4 \cdot H_2O$ impurity.

11

Upon Li extraction, the general structural framework composed of FeO_6 octahedra and SO_4 tetrahedra is preserved, while the position of Li2 slightly changes (Table 1,Table 2 and Table 3 and Figure 5) so that its coordination is decreased from five-fold in the pristine material to three-fold in $Li_{1.5}Fe(SO_4)_2$. During the oxidation process, a slight contraction of the structure is observed, since the refined cell parameters vary from a=9.2798(8) Å , b=9.2089(11) Å and c=13.6765(14) Å for $Li_2Fe(SO_4)_2$ to a=9.1776(3) Å, b=9.045(3) Å and to c=13.612(4) Å for $Li_{1.5}Fe(SO_4)_2$ and a=9.1576(5) Å, b=8.9162(5) Å and c=13.3978(8) Å for $Li_{1.0}Fe(SO_4)_2$. The volume change between these three phases is linear and results in an overall volume change of merely ΔV/V=7%, which is less pronounced than for the monoclinic phase (ΔV/V=12%) (Figure 2d).
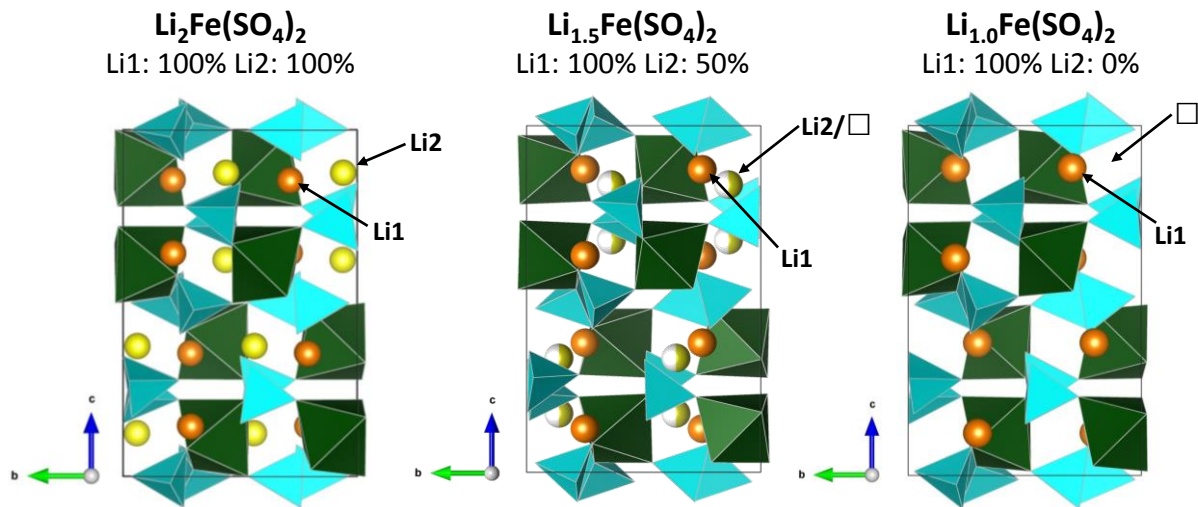
Figure 5: Comparison of the structures $Li_2Fe(SO_4)_2$, $Li_{1.5}Fe(SO_4)_2$ and $Li_{1.0}Fe(SO_4)_2$. The FeO_6 octahedra and SO_4 tetrahedra are displayed in green and blue, respectively. Lithium atoms in the Li1 site are illustrated as orange balls and in Li2 sites as yellow balls. In $Li_{1.5}Fe(SO_4)_2$ the half delithiated Li2 site is represented through half-colored white-yellow balls.

In order to gain more insight into the influence of different Li-vacancy arrangements on the stability of phases $Li_xFe(SO_4)_2$ (x = 2.0, 1.5, 1.0), we calculated a range of Li-vacancy configurations using DFT. Figure SI 1 compares the internal coordinates (position of Li atoms and orientation of FeO_6 octahedra and SO_4 tetrahedra) of the phases $Li_xFe(SO_4)_2$ determined from NPD data and the structure of the ground states calculated using DFT. The agreement between experiment and theory is good, especially for $Li_{1.0}Fe(SO_4)_2$ and $Li_{2.0}Fe(SO_4)_2$. The DFT optimized lattice constants (Table 4) are also within the expected deviation range for PBE+U calculations (differences are less than 2.5 %); this slight difference is easily explained by the usual propensity of DFT relaxation to expand the unit cell when using a generalized

gradient approximation functional such as PBE. The atomic positions deduced by DFT for the phases $Li_xFe(SO_4)_2$ (x = 2.0, 1.5, 1.0) are listed in Tables SI 1, SI 2 and SI 3. In agreement with the interpretation of the NPD results discussed above, our DFT calculations reveal that Li atoms in $Li_{1.0}Fe(SO_4)_2$ prefer to occupy all the Li1 sites, leaving the remaining Li2 sites empty (structure A in Figure 6). The opposite configuration with all of the Li2 sites occupied (structure D in Figure 6) appears at significantly higher energy (106 meV/f.u.). In addition, other possible configurations with mixed occupations of Li1 and Li2 sites (for example structures B and C in Figure 6) are less stable than the ground state by at least 20 meV/f.u.

For $Li_{1.5}Fe(SO_4)_2$, DFT results also confirm that structures with fully-occupied Li1 sites and half-occupied Li2 sites are energetically more favourable (structures A and B in Figure 7). However, a key observation is that some of these Li-vacancy configurations are substantially less preferred than others. For example, structure D in Figure 7 has fully occupied Li1 sites and half occupied Li2 sites, but it is 33 meV/f.u. less stable than the ground-state structure. This suggests that Li atoms are probably not randomly distributed within the Li2 sublattice, with preference for some particular Li-vacancy arrangements. Note that NPD experiments do not confirm such a preferential occupation in the Li2 sublattice as no superstructure peaks have been observed. However, taking into account half-occupied Li2 sites by DFT would require prohibitive computational resources.
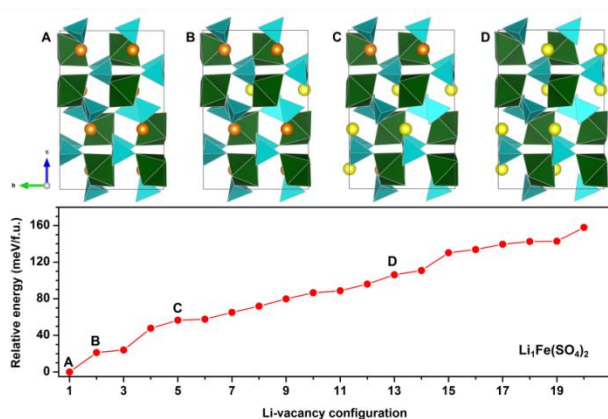
Figure 6: Relative energies (in meV per formula unit) of the 20 most stable Li-vacancy configurations in $Li_{1.0}Fe(SO_4)_2$ using DFT. Inset A shows the optimized structure of the most stable configuration. Insets B, C, and D show some selected high-energy configurations. Color code: Li atom in a Li1 site, orange; Li atom in a Li2 site, yellow; SO_4 tetrahedra, light blue; FeO_6 octahedra, dark green.

13
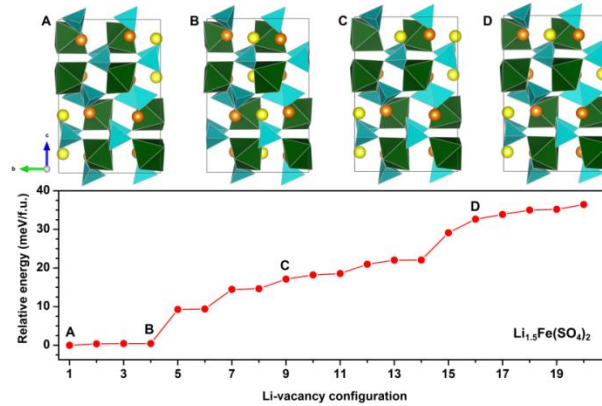
Figure 7: Relative energies (in meV per formula unit) of the 20 most stable Li-vacancy configurations in Li$_{1.5}$Fe(SO$_4$)$_2$ using DFT. Inset A shows the optimized structure of the most stable configuration. Insets B, C, and D show some selected high-energy configurations. Color code: Li atom in a Li1 site, orange; Li atom in a Li2 site, yellow; SO$_4$ tetrahedra, light blue; FeO$_6$ octahedra, dark green.

Going back to the polarization in the V=f(x) curve, previous studies have discussed the feasibility of a SO$_4$-paddle-wheel mechanism to account for differences in the ionic conductivity of sulfate-based compounds.[42] Since NPD experiments did not reveal any of such paddle-wheel features for the monoclinic neither for the orthorhombic polymorph, which show ionic conductivities at room temperature of σ_{RT}=2.6 x 10^{-18} S/cm and σ_{RT}=2.2 x 10^{-14} S/cm, respectively, we decided to explore the Li ionic diffusion paths via bond valence energy landscape (BVEL) calculations obtained by transforming valence units into energy units as implemented in the program BondSTR of the FullProf Suite.[25,45] Calculations were made using the soft bond valence parameters developed by S. Adams.[45] These BVEL calculations take into account the polarizability of the mobile species (here Li$^+$) and the influence of the counter-ions up to a certain distance which was set here at 8 Å. The BVEL maps calculated for both Li$_2$Fe(SO$_4$)$_2$ polymorphs (Figure 8) reveal 3D conduction pathways for the monoclinic as well as for the orthorhombic phase. The energies necessary to obtain an infinitely connected network in at least one direction are in the same range for the two polymorphs and account for 1.04 eV for the monoclinic and 1.11 eV for the orthorhombic phase as compared to 1.54 eV and 1.19 eV determined experimentally by a.c. impedance.[21]

Further exploiting BVEL calculations, we note that in orthorhombic Li$_2$Fe(SO$_4$)$_2$, the Li1 site is slightly lower in energy than the Li2 site, which is in qualitative agreement with the preferential delithiation of Li2 as deduced by NPD experiments and DFT results. In the monoclinic structure, however, there is a unique crystallographic site for Li and therefore all the Li atoms behave homogeneously. Nevertheless, the BVEL maps collected for the monoclinic structure disclose a local minimum in the 3D diffusion path around the

14

position (½, 0, ½), which becomes lower in energy than the original Li site (Figure SI 2) in the structure of the delithiated phase and which indeed corresponds to the Li position in the delithiated monoclinic phase $Li_1Fe(SO_4)_2$ that was reported previously from NPD data.[18]

Overall, BVEL like NPD fail to determine the origin of the difference in polarization between the two polymorphs suggesting another origin aside the structural one. Among the various possibilities is the role of defects together with grain boundaries. At this point, we should recall our difficulties in achieving a pure monoclinic phase due to the remaining presence of minute amount of amorphous orthorhombic material. We believe that such developed grain boundaries could be responsible for the lower conductivity of the monoclinic polymorph. Such a scenario would be transparent to BVEL calculations. Lastly, another possibility could come from electronic conductivity. Hence, our reason to measure the material band gap via UV/Vis spectroscopy, which besides accounting for the color of a material could give qualitative information about the material electronic behavior.

a) BVEL activation energy of monoclinic $Li_2Fe(SO_4)_2$: 1.04 eV

b) BVEL activation energy of orthorhombic $Li_2Fe(SO_4)_2$: 1.11 eV
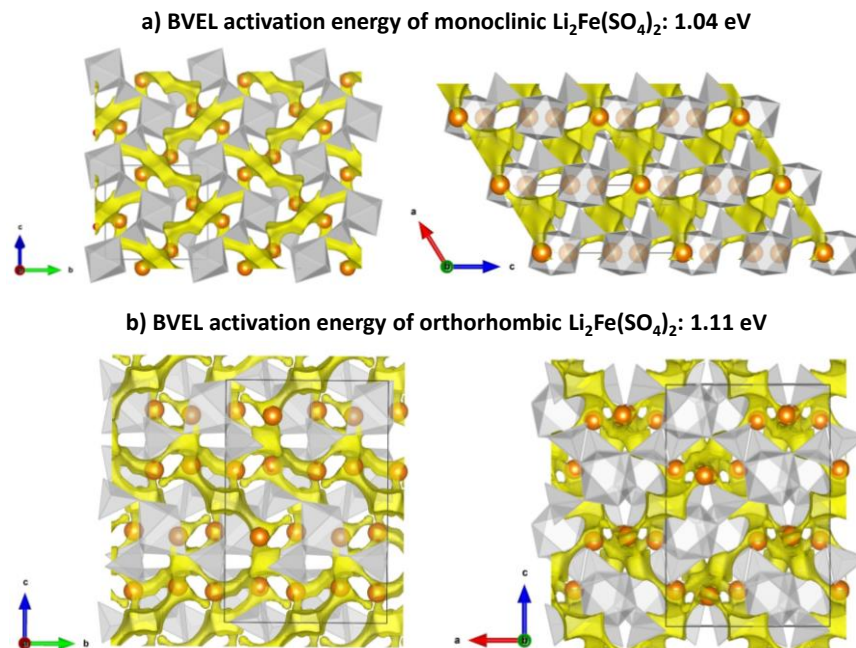
Figure 8: BVEL maps of monoclinic (top) and orthorhombic (bottom) $Li_2Fe(SO_4)_2$. Grey polyhedra represent the SO_4 tetrahedra and FeO_6 octahedra of the main frameworks of the structures, orange balls indicate the position of the Li atoms as found experimentally, yellow volumes represent the volume of stability of a Li atom for the given energy cut-off (indicated in the figure). For the plots shown here the chosen cut-off values lie 0.5 eV above the energies (1.04 eV for monoclinic $Li_2Fe(SO_4)_2$ and 1.11 eV for orthorhombic $Li_2Fe(SO_4)_2$).

Band gap measurements of the $Li_2M(SO_4)_2$ phases (M = Mn, Fe, Co, Ni, Zn)

A first hint about the electronic behavior of the orthorhombic and monoclinic $Li_2M(SO_4)_2$ (M = Mn, Fe, Co, Ni, Zn) compounds can already be obtained from the distinctive colors (top Figure 9) of these phases, which indicate that the $Li_2M(SO_4)_2$ phases are insulators. In order to be able to assign the observed colors to the respective electron d-d transitions using the Tanabe-Sugano diagrams,[46] UV/Vis spectroscopy was performed in the range of 200-1500 nm (~0.8-6 eV) (Figure 9). In the visible light region, the absorption peak observed for the orthorhombic $Li_2Ni(SO_4)_2$ at ~3.0 eV, attributed to the $^3A_2$ to $^3T_1$ transition, is in agreement with its yellow color, while the pink color of the two polymorphs of $Li_2Co(SO_4)_2$ is attributed to the $^4T_1$ to $^4T_{1g}$ transition at around 2.3 eV. On the other hand, $Li_2Fe(SO_4)_2$ and $Li_2Mn(SO_4)_2$ show a slight absorption over the whole visible light domain without any distinct absorption peak, which leads to their beige/brownish color. Similarly, the white $Li_2Zn(SO_4)_2$ shows almost no absorption in the visible range.
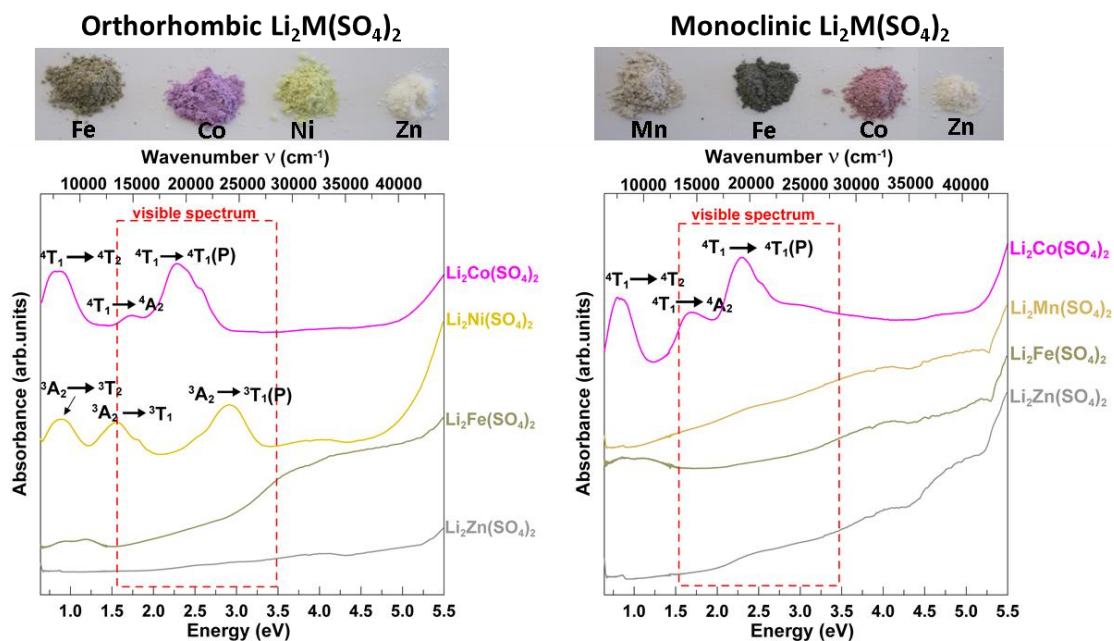
Figure 9: On the top, pictures of the powder samples of the orthorhombic and monoclinic $Li_2M(SO_4)_2$ (M = Mn, Fe, Co, Ni, Zn) compounds illustrating the different colors depending on the 3d transition metal. On the bottom, UV/Vis spectra of the orthorhombic and monoclinic $Li_2M(SO_4)_2$ series.

For the calculation of the optical band gap E_g from the UV/Vis measurements, we used the Kubelka-Munk formalism $f(R) = (1-R)^2/2R = K/s$, where R is the reflectance, K the absorption coefficient and s the scattering coefficient.[47] Plotting $(f(R)*h\nu)^n$ against the energy, with n=1/2 for an indirect or n=2 for a direct band gap, is commonly used to determine E_g.[48] Both formulae gave similar results for E_g for the various

Li$_2$M(SO$_4$)$_2$ (M = Mn, Fe, Co, Ni, Zn) phases, as already observed in the literature for other compounds.[48] In the following, we assumed a direct band gap and therefore used the equation (f(R)*hv)^2. Figure 10 illustrates the Kubelka-Munk plot for the orthorhombic and monoclinic Li$_2$Co(SO$_4$)$_2$ and Li$_2$Fe(SO$_4$)$_2$ phases. The obtained optical band gap values for the various compounds (Table SI 4) are all in the range between 5.2 and 5.5 eV, which is higher than what has been reported for other polyanionic materials such as LiFePO$_4$ (3.7 eV), Li$_2$FeSiO$_4$ (3.7 eV) and LiFeSO$_4$F (2.8-3.6 eV, depending on the polymorph and the calculation method).[49–54] The reason for the large band gaps for the Li$_2$M(SO$_4$)$_2$ polymorphs is nested in their specific structures, as it has also been observed for LiFePO$_4$.[49] Such large optical band gaps would naively lead to the expectation of having an electronic band gap with an activation energy of ~ 2.5 eV (5 eV/2), which is quite higher than the activation energies (~0.9 eV) deduced by a.c.-d.c. impedance measurements. In this case, such compounds could not be used as electrodes due to their insulating character. It should be noted that a similar situation was found for LiFePO$_4$, which shows an optical gap of 3.8 eV as opposed to an activation energy of solely ~0.5 eV.[49] It is therefore quite likely that polaron-type models, used to describe transport properties in LiFePO$_4$[49], could also be applied to Li$_2$Fe(SO$_4$)$_2$.
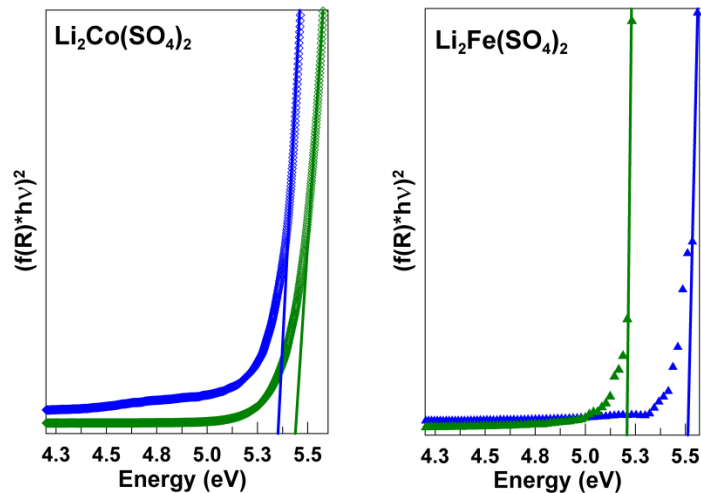
Figure 10: Kubelka-Munk functions for Li$_2$Co(SO$_4$)$_2$ (left) and Li$_2$Fe(SO$_4$)$_2$ (right). The blue symbols refer to the monoclinic polymorph and the green ones to the orthorhombic phases.

The enhanced electrochemical performance of the orthorhombic polymorph as compared to its monoclinic counterpart led us to explore the feasibility of enlarging the orthorhombic Li$_2$M(SO$_4$)$_2$ family, which already counts several members (Fe, Co, Zn and Ni), by Mn, which has been so far solely stabilized in its monoclinic form.[21] Based on the fact that the monoclinic phases are less dense (e.g larger volumes) we decided to explore the use of pressure to transform the low-density monoclinic Li$_2$M(SO$_4$)$_2$ polymorph

17

into the high-density orthorhombic one for the Co and Mn members solely. Therefore pressure experiments were performed using a diamond anvil cell (DAC) that was loaded with the monoclinic $Li_2Co(SO_4)_2$ polymorph and the transformation was followed by Raman spectroscopy while gradually increasing the pressure of the DAC. Reference Raman spectra recorded for both monoclinic and orthorhombic phases of $Li_2Co(SO_4)_2$ and for monoclinic $Li_2Mn(SO_4)_2$ (Figure SI 3) show several peaks that could be attributed to different SO_4 modes, where v_1 and v_3 correspond to stretching modes and v_2 and v_4 to bending modes. Figure 11a shows that the Raman spectra of monoclinic $Li_2Co(SO_4)_2$ progressively change with increasing pressure. Beyond 3.65 GPa and onwards the Raman spectra become very similar to the one of the orthorhombic phase implying its structural conversion. The same experiment was performed with a DAC loaded with monoclinic $Li_2Mn(SO_4)_2$. Figure 11b shows that from 3 GPa onwards, the Raman spectra evolve with increasing pressure in a similar way as the cobalt system suggesting the feasibility to transform the Mn-based polymorph as well. However, caution has to be exercised here as we obviously do not have the Raman spectra for the Mn-based orthorhombic polymorph. High pressure *insitu* XRD measurements are being planned to confirm this finding.
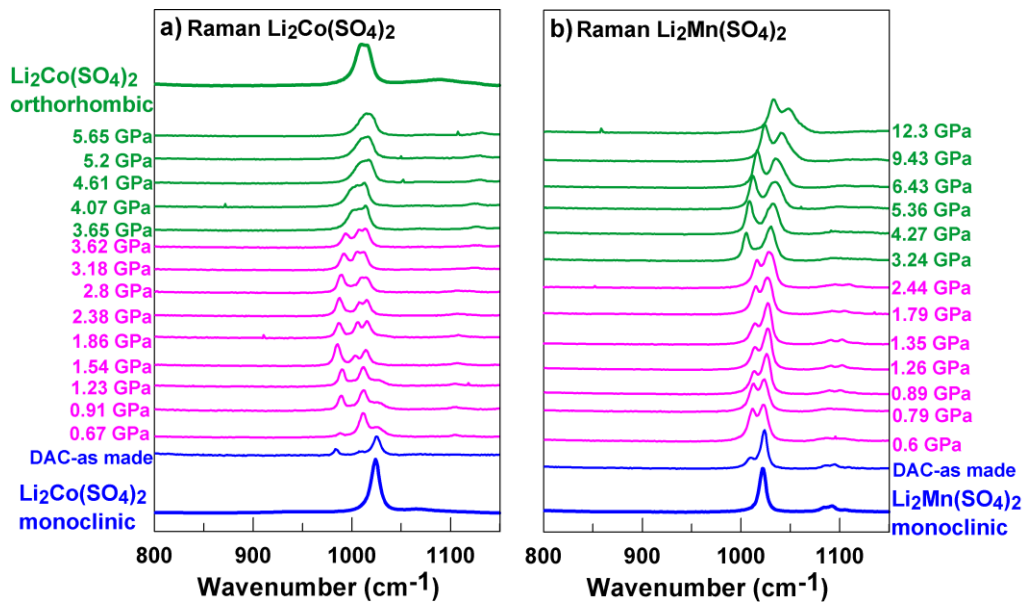

Figure 11: Evolution of the Raman spectra of a) $Li_2Co(SO_4)_2$ and b) $Li_2Mn(SO_4)_2$ loaded in a Diamond Anvil cell as a function of the increasing pressure.

18

Conclusion

Using neutron diffraction experiments coupled with DFT calculations for orthorhombic $Li_2Fe(SO_4)_2$, we could unambiguously deduce that upon electrochemically oxidation the Li2 cation is progressively removed leading to the stabilization of a distinct intermediate phase $Li_{1.5}Fe(SO_4)_2$ prior to forming the delithiated phase $Li_{1.0}Fe(SO_4)_2$. The Li1 site, on the other hand, stays fully lithiated, which was also confirmed by DFT and BVEL calculations showing that the Li1 site is significantly lower in energy than the Li2 site. Neither BVEL energy values nor band gap energies could account for the difference in polarization, which hints for an important role of defects and/or grain boundaries in these polymorphs that might influence their conducting properties. The influence of extrinsic properties such as defects would also explain why even though $Li_2Fe(SO_4)_2$ presents a large band gap of ~5 eV as deduced by UV/Vis spectroscopy, we do not need any carbon coating for electrochemical cycling in contrast to $LiFePO_4$, which presents a band gap of merely 3.7 eV. However, the impact of defects on the conduction properties of both polymorphs needs to be studied in more details. Based on our pressure experiment results, the effect of pressure on other polyanionic polymorph systems is being explored.

Acknowledgements

19

Supporting Information

Structures and structural parameters for orthorhombic $Li_xFe(SO_4)_2$ (x = 2.0, 1.5, 1.0) determined from DFT calculations, BVEL maps for monoclinic $Li_2Fe(SO_4)_2$, Band gap energies for monoclinic and orthorhombic $Li_2M(SO_4)_2$ phases, Raman spectra of $Li_2Mn(SO_4)_2$ and $Li_2Co(SO_4)_2$, cif files of orthorhombic $Li_xFe(SO_4)_2$ (x = 2.0, 1.5, 1.0) from neutron powder diffraction data.

References

1   C. Masquelier and L. Croguennec, *Chem. Rev.*, 2013, **113**, 6552–6591.
2   A. K. Padhi, K. S. Nanjundaswamy and J. B. Goodenough, *J. Electrochem. Soc.*, 1997, **144**, 1188–1194.
3   A. K. Padhi, V. Manivannan and J. B. Goodenough, *J. Electrochem. Soc.*, 1998, **145**, 1518–1520.
4   V. Legagneur, Y. An, A. Mosbah, R. Portal, A. Le Gal La Salle, A. Verbaere, D. Guyomard and Y. Piffard, *Solid State Ion.*, 2001, **139**, 37–46.
5   A. Yamada, N. Iwane, Y. Harada, S. Nishimura, Y. Koyama and I. Tanaka, *Adv. Mater.*, 2010, **22**, 3583–3587.
6   L. Tao, G. Rousse, J. N. Chotard, L. Dupont, S. Bruyère, D. Hanžel, G. Mali, R. Dominko, S. Levasseur and C. Masquelier, *J. Mater. Chem. A*, 2014, **2**, 2060–2070.
7   A. Abouimrane, N. Ravet, M. Armand, A. Nytén and J. Thomas, *12th Int. Meet. Lithium Batter. Nara Jpn. - Abstr. N°350*, 2004.
8   A. Nytén, A. Abouimrane, M. Armand, T. Gustafsson and J. O. Thomas, *Electrochem. Commun.*, 2005, **7**, 156–160.
9   M. S. Islam, R. Dominko, C. Masquelier, C. Sirisopanaporn, A. R. Armstrong and P. G. Bruce, *J. Mater. Chem.*, 2011, **21**, 9811–9818.
10 C. Sirisopanaporn, C. Masquelier, P. G. Bruce, A. R. Armstrong and R. Dominko, *J Am Chem Soc*, 2010, **133**, 1263–1265.
11 N. Recham, J.-N. Chotard, L. Dupont, C. Delacourt, W. Walker, M. Armand and J.-M. Tarascon, *Nat. Mater.*, 2010, **9**, 68–74.
12 P. Barpanda, M. Ati, B. C. Melot, G. Rousse, J.-N. Chotard, M.-L. Doublet, M. T. Sougrati, S. A. Corr, J.-C. Jumas and J.-M. Tarascon, *Nat. Mater.*, 2011, **10**, 772–779.
13 M. Ati, B. C. Melot, J.-N. Chotard, G. Rousse, M. Reynaud and J.-M. Tarascon, *Electrochem. Commun.*, 2011, **13**, 1280–1283.
14 M. Ati, M. Sathiya, S. Boulineau, M. Reynaud, A. M. Abakumov, G. Rousse, B. C. Melot, G. Van Tendeloo and J.-M. Tarascon, *J. Am. Chem. Soc.*, 2012, **134**, 18380–18387.
15 M. Reynaud, P. Barpanda, G. Rousse, J.-N. Chotard, B. C. Melot, N. Recham and J.-M. Tarascon, *Solid State Sci.*, 2012, **14**, 15–20.
16 M. Reynaud, M. Ati, B. C. Melot, M. T. Sougrati, G. Rousse, J.-N. Chotard and J.-M. Tarascon, *Electrochem. Commun.*, 2012, **21**, 77–80.
17 M. Reynaud, M. Ati, S. Boulineau, M. T. Sougrati, B. C. Melot, G. Rousse, J.-N. Chotard and J.-M. Tarascon, *ECS Trans.*, 2013, **50**, 11–19.
18 M. Reynaud, G. Rousse, J.-N. Chotard, J. Rodríguez-Carvajal and J.-M. Tarascon, *Inorg. Chem.*, 2013, **52**, 10456–10466.

19 M. Reynaud, G. Rousse, M. Abakumov, M.-T. Sougrati, G. Van Tendeloo, J.-N. Chotard and J.-M. Tarascon, *J. Mater. Chem. A*, 2013, **2**, 2671–2680.

20 M. Reynaud, Design of new sulfate-based positive electrode materials for Li- and Na-ion batteries / Elaboration de nouveaux matériaux à base de sulfates pour l'électrode positive des batteries à ions Li et Na. Ph.D. dissertation, Université de Picardie Jules Verne: Amiens (France), 2013. Available at https://tel.archives-ouvertes.fr/tel-01018912.

21 L. Lander, M. Reynaud, G. Rousse, M. T. Sougrati, C. Laberty-Robert, R. J. Messinger, M. Deschamps and J.-M. Tarascon, *Chem. Mater.*, 2014, **26**, 4178–4189.

22 L. Lander, T. Hansen, M. Reynaud, J. Rodriguez-Carvajal, G. Rousse, M. Sun and J.-M. Tarascon, 2014. Institut Laue-Langevin (ILL) doi:10.5291/ILL-DATA.5-31-2328.

23 H. M. Rietveld, *J. Appl. Crystallogr.*, 1969, **2**, 65–71.

24 J. Rodríguez-Carvajal, *Physica B Condens. Matter*, 1993, **192**, 55–69.

25 J. Rodríguez-Carvajal, *FullProf Suite*, https://www.ill.eu/sites/fullprof/.

26 J. C. Chervin, B. Canny, J. M. Besson and P. Pruzan, *Rev. Sci. Instrum.*, 1995, **66**, 2595–2598.

27 B. Couzinet, N. Dahan, G. Hamel and J.-C. Chervin, *High Press. Res.*, 2003, **23**, 409–415.

28 J. C. Chervin, B. Canny and M. Mancinelli, *High Press. Res.*, 2001, **21**, 305–314.

29 J. D. Barnett, S. Block and G. J. Piermarini, *Rev. Sci. Instrum.*, 1973, **44**, 1–9.

30 V. V. Strelchuk, O. F. Kolomys, B. O. Golichenko, M. I. Boyko, E. B. Kaganovich, I. M. Krishchenko, S. O. Kravchenko, O. S. Lytvyn, E. G. Manoilov and I. M. Nasieka, *Semicond. Phys. Quantum Electron. Optoelectron.*, 2015, 46–52.

31 A. Paolone, A. Sacchetti, T. Corridoni, P. Postorino, R. Cantelli, G. Rousse and C. Masquelier, *Solid State Ion.*, 2004, **170**, 135–138.

32 J. P. Perdew, A. Ruzsinszky, G. I. Csonka, O. A. Vydrov, G. E. Scuseria, L. A. Constantin, X. Zhou and K.Burke, *Phys. Rev. Lett.*, 2008, **100**, 136406.

33 G. Kresse and J. Furthmüller, *Phys. Rev. B*, 1996, **54**, 11169–11186.

34 G. Kresse, M. Marsman and J. Furthmüller, *VASP (Vienna Ab-initio Simulation Package)*, https://www.vasp.at/.

35 G. Kresse and D. Joubert, *Phys. Rev. B*, 1999, **59**, 1758–1775.

36 S. L. Dudarev, G. A. Botton, S. Y. Savrasov, C. J. Humphreys and A. P. Sutton, *Phys. Rev. B*, 1998, **57**, 1505–1509.

37 G. Hautier, A. Jain, T. Mueller, C. Moore, S. P. Ong and G. Ceder, *Chem. Mater.*, 2013, **25**, 2064–2074.

38 J. Clark, C. Eames, M. Reynaud, G. Rousse, J.-N. Chotard, J.-M. Tarascon and M. S. Islam, *J. Mater. Chem. A*, 2014, **2**, 7446–7453.

39 M. Reynaud, J. Rodríguez-Carvajal, J.-N. Chotard, J.-M. Tarascon and G. Rousse, *Phys. Rev. B*, 2014, **89**, 104419.

40 A. Van der Ven, J. C. Thomas, Q. Xu, B. Swoboda and D. Morgan, *Phys. Rev. B*, 2008, **78**, 104306.

41 P. P. Ewald, *Ann. Phys.*, 1921, **369**, 253–287.

42 R. Jalem, M. J. D. Rushton, W. Manalastas, M. Nakayama, T. Kasuga, J. A. Kilner and R. W. Grimes, *Chem. Mater.*, 2015, **27**, 2821–2831.

43 L. J. Miara, W. D. Richards, Y. E. Wang and G. Ceder, *Chem. Mater.*, 2015, **27**, 4040–4047.

44 A. Lundén, *Solid State Commun.*, 1988, **65**, 1237–1240.

45 S. Adams, *Solid State Ion.*, 2006, **177**, 1625–1630.

46 Y. Tanabe and S. Sugano, *J. Phys. Soc. Jpn.*, 1954, **9**, 766–779.

47 P. Kubelka, *J. Opt. Soc. Am.*, 1948, **38**, 448–448.

48 R. López and R. Gómez, *J. Sol-Gel Sci. Technol.*, 2012, **61**, 1–7.

49 F. Zhou, K. Kang, T. Maxisch, G. Ceder and D. Morgan, *Solid State Commun.*, 2004, **132**, 181–186.

50 L.-L. Zhang, H.-B. Sun, X.-L. Yang, Y.-W. Wen, Y.-H. Huang, M. Li, G. Peng, H.-C. Tao, S.-B. Ni and G. Liang, *Electrochimica Acta*, 2015, **152**, 496–504.

21

51 Y. Xie, H.-T. Yu, T.-F. Yi, Q. Wang, Q.-S. Song, M. Lou and Y.-R. Zhu, *J Mater Chem A*, 2015, **3**, 19728–19737.

52 Z. Liu and X. Huang, *Solid State Ion.*, 2010, **181**, 1209–1213.

53 C. Frayret, A. Villesuzanne, N. Spaldin, E. Bousquet, J.-N. Chotard, N. Recham and J.-M. Tarascon, *Phys Chem Chem Phys*, 2010, **12**, 15512–15522.

54 S. C. Chung, P. Barpanda, S. Nishimura, Y. Yamada and A. Yamada, *Phys. Chem. Chem. Phys.*, 2012, **14**, 8678–8682.

Tables

Table 1: Crystallographic data and atomic positions of the orthorhombic Li$_2$Fe(SO$_4$)$_2$ determined from Rietveld refinements of its neutron powder diffraction pattern recorded at 30 K. All atoms belonging to the same chemical species were considered to have the same B$_{iso}$.

				Orthorhombic Li$_2$Fe(SO$_4$)$_2$				
Space group P b c a			R$_{Bragg}$ = 2.48 %				χ^2 = 5.57	
a = 9.2798(9) Å		*b* = 9.2089(11) Å	*c* = 13.6765(14) Å				*V* = 1168.8(3) Å^3	
Atom	Wyckoff position	Occupancy	*x/a*	*y/b*	*z/c*	B$_{iso}$ (Å^2)	BVS
Li1	8*c*	1.0	0.489(7)	0.712(7)	0.355(5)	1.3(2)	0.91(8)
Li2	8*c*	1.0	0.747(6)	0.560(5)	0.624(5)	1.3(2)	1.20(9)
Fe	8*c*	1.0	0.8635(12)	0.6024(14)	0.3763(10)	0.62(4)	2.06(5)
S1	8*c*	1.0	0.6600(14)	0.8129(13)	0.5109(10)	1.20(11)	5.67(14)
S2	8*c*	1.0	0.5777(15)	0.4250(15)	0.2734(10)	1.20(11)	5.70(15)
O1	8*c*	1.0	0.5010(13)	0.8005(19)	0.5198(12)	0.84(2)	1.90(8)
O2	8*c*	1.0	0.7107(17)	0.9667(13)	0.4997(12)	0.84(2)	1.95(8)
O3	8*c*	1.0	0.687(2)	0.7288(16)	0.4193(10)	0.84(2)	2.00(8)
O4	8*c*	1.0	0.7455(17)	0.7411(18)	0.5904(11)	0.84(2)	1.90(10)
O5	8*c*	1.0	0.4847(16)	0.500(2)	0.3470(11)	0.84(2)	1.80(10)
O6	8*c*	1.0	0.533(2)	0.4643(17)	0.1720(9)	0.84(2)	2.01(8)
O7	8*c*	1.0	0.5684(19)	0.2633(12)	0.2786(14)	0.84(2)	2.06(9)
O8	8*c*	1.0	0.7294(15)	0.478(3)	0.2780(13)	0.84(2)	1.91(9)

Table 2: Crystallographic data and atomic positions of the orthorhombic $Li_{1.5}Fe(SO_4)_2$ determined from Rietveld refinements of its neutron powder diffraction pattern recorded at 100 K. All atoms belonging to the same chemical species were considered to have the same B_{iso}.

Orthorhombic $Li_{1.5}Fe(SO_4)_2$

Space group $P\,b\,c\,a$			R_{Bragg} = 3.87 %			χ^2 = 40.1	
a = 9.1776(3) Å	b = 9.049(3) Å		c = 13.612(4) Å			V = 1130.4(6) Å^3	

Atom	Wyckoff position	Occupancy	x/a	y/b	z/c	B_{iso} (Å^2)	BVS
Li1	8c	1.0	0.464(16)	0.750(19)	0.374(14)	0.3(2)	1.17(3)
Li2	8c	0.5	0.69(3)	0.64(3)	0.670(2)	0.3(2)	1.1(5)
Fe	8c	1.0	0.846(4)	0.606(4)	0.3650(3)	1.08(16)	2.69(18)
S1	8c	1.0	0.6265(14)	0.8080(14)	0.5102(10)	0.8(3)	5.59(3)
S2	8c	1.0	0.5905(14)	0.4411(16)	0.2683(10)	0.8(3)	5.63(3)
O1	8c	1.0	0.4667(2)	0.789(6)	0.528(5)	1.33(7)	1.99(15)
O2	8c	1.0	0.646(6)	0.9629(3)	0.473(4)	1.33(7)	1.94(15)
O3	8c	1.0	0.637(19)	0.719(5)	0.4175(2)	1.33(7)	2.13(3)
O4	8c	1.0	0.74267(4)	0.782(6)	0.586(3)	1.33(7)	1.76(2)
O5	8c	1.0	0.493(4)	0.489(6)	0.3507(3)	1.33(7)	1.59(18)
O6	8c	1.0	0.527(5)	0.496(6)	0.1738(2)	1.33(7)	1.99(17)
O7	8c	1.0	0.587(5)	0.2768(18)	0.282(4)	1.33(7)	2.04(14)
O8	8c	1.0	0.7506(2)	0.471(6)	0.273(5)	1.33(7)	2.16(2)

Table 3: Crystallographic data and atomic positions of the orthorhombic $Li_{1.0}Fe(SO_4)_2$ determined from Rietveld refinements of its neutron powder diffraction pattern recorded at 100 K. All atoms belonging to the same chemical species were considered to have the same B_{iso}.

Orthorhombic $Li_{1.0}Fe(SO_4)_2$

Space group $P\ b\ c\ a$				R_{Bragg} = 2.67 %		χ^2 = 4.68	
a = 9.1576(5) Å	b =8.9162(5) Å			c = 13.3978(8) Å		V = 1093.95(11) Å^3	
Atom	Wyckoff position	Occupancy	x/a	y/b	z/c	B_{iso} (Å^2)	BVS
Li1	8c	1.0	0.442(5)	0.702(5)	0.379(3)	0.34(19)	1.06(6)
Li2	8c	0.0	-	-	-	-	-
Fe	8c	1.0	0.8591(10)	0.6076(10)	0.3719(7)	0.54(4)	3.08(6)
S1	8c	1.0	0.652(3)	0.813(3)	0.5062(19)	0.41(6)	6.0(3)
S2	8c	1.0	0.581(3)	0.436(3)	0.274(2)	0.41(6)	6.0(3)
O1	8c	1.0	0.4973(15)	0.7929(13)	0.5265(9)	0.511(15)	2.17(14)
O2	8c	1.0	0.6880(12)	0.9740(14)	0.4881(10)	0.511(15)	2.13(10)
O3	8c	1.0	0.6895(15)	0.7271(15)	0.4173(9)	0.511(15)	2.22(12)
O4	8c	1.0	0.7403(13)	0.7663(16)	0.5956(10)	0.511(15)	2.07(12)
O5	8c	1.0	0.4882(15)	0.4977(15)	0.3530(10)	0.511(15)	1.95(13)
O6	8c	1.0	0.5199(14)	0.4773(14)	0.1760(8)	0.511(15)	2.20(13)
O7	8c	1.0	0.5854(13)	0.2701(13)	0.2742(10)	0.511(15)	2.14(12)
O8	8c	1.0	0.7301(14)	0.4964(16)	0.2775(10)	0.511(15)	2.23(13)

Table 4: Comparison of the cell parameters of orthorhombic $Li_xFe(SO_4)_2$ (x = 2.0, 1.5, 1.0) obtained from DFT calculation and deduced from experimental neutron powder diffraction (NPD) measurements.

	$Li_{2.0}Fe(SO_4)_2$		$Li_{1.5}Fe(SO_4)_2$		$Li_{1.0}Fe(SO_4)_2$	
	DFT	NPD	DFT	NPD	DFT	NPD
a (Å)	9.3738	9.2798(9)	9.3651	9.178(3)	9.2941	9.1576(5)
b (Å)	9.3078	9.2089(11)	9.1963	9.049(3)	9.0511	8.9162(5)
c (Å)	13.8328	13.6765(14)	13.8307	13.613(5)	13.7374	13.3978(8)
V ($Å^3$)	1206.90	1168.8(3)	1191.16	1130.6(7)	1155.62	1093.95(11)